Yuan, Xiaolei; Xu, Xinjie; Liu, Jinxiang; Pan, Yiqun; Kosonen, Risto; Gao, Yang

Improvement in airflow and temperature distribution with an in-rack UFAD system at a high-density data center

Published in:
Building and Environment

DOI:
10.1016/j.buildenv.2019.106495

Published: 15/01/2020

Document Version
Peer-reviewed accepted author manuscript, also known as Final accepted manuscript or Post-print

Journal Pre-proof

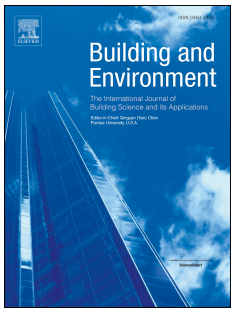

Improvement in airflow and temperature distribution with an in-rack UFAD system at a high-density data center

Xiaolei Yuan, Xinjie Xu, Jinxiang Liu, Yiqun Pan, Risto Kosonen, Yang Gao

PII: S0360-1323(19)30707-3

DOI: https://doi.org/10.1016/j.buildenv.2019.106495

Reference: BAE 106495

To appear in: *Building and Environment*

Received Date: 22 July 2019

Revised Date: 21 October 2019

Accepted Date: 23 October 2019

Please cite this article as: Yuan X, Xu X, Liu J, Pan Y, Kosonen R, Gao Y, Improvement in airflow and temperature distribution with an in-rack UFAD system at a high-density data center, *Building and Environment* (2019), doi: https://doi.org/10.1016/j.buildenv.2019.106495.

Improvement in airflow and temperature distribution with an in-rack UFAD system at a high-density data center

Xiaolei Yuan[a,c], Xinjie Xu[b], Jinxiang Liu[b,*],Yiqun Pan[a,*], Risto Kosonen[b,c], Yang Gao[d]

[a] School of Mechanical Engineering, Tongji University, 4800 Cao'an Road, 201804 Shanghai, China

[b] College of Urban Construction, Nanjing Tech University, P.O. Box 76, 210009 Nanjing, China

[c] School of Engineering, Aalto University, P.O. Box 14400, FI-00076 Espoo, Finland

[d]Nanjing Yangtze River Urban Architectural Design Co., LTD 210002 Nanjing, China

*Corresponding Author.

E-mail address：jxliu@njut.edu.cn (J. Liu)

yiqunpan@tongji.edu.cn (Y. Pan)

Abstract

This paper introduced and analyzed a new concept where an under-floor air supply (UFAD) system with cold aisle containment (CAC) is replaced by a new in-rack UFAD system called an in-rack cold aisle (IR-CA). The IR-CA system is analyzed using CFD simulation, and on-site measurement was carried out to validate the feasibility and reliability of simulation models. The study is divided into eight cases with seven different dimensions for the rack air inlet (2.2 m × 0.6 m, 0.2 m × 0.6 m, 0.3 m × 0.6 m, 0.4 m × 0.6 m, 0.5 m × 0.6 m, 0.6 m × 0.6 m, and 0.7 m × 0.6 m), while an additional partition plane is placed in Case 8 with a 0.6 m × 0.6-m in-rack air inlet. The thermal distribution is compared and analyzed in the eight cases, while cooling efficiency and energy saving is compared between the original and optimal cases. The results showed that the optimal thermal distribution is achieved in Case 8 with a 0.6 m × 0.6 m IR-CA and partition plane, while the thermal distribution in Case 8 with SAT of 23 □ is still much better than that in the original DC. The application of a 0.6 m × 0.6 m IR-CA and partition plane can save approximately 98 kWh/day in electricity consumption in the studied DC. A new evaluation index named the MS index is proposed to evaluate the optimization effects of the optimization model based on the original model.

Keywords: Data centers, Airflow management, In-rack UFAD, Temperature distribution, Velocity distribution, energy saving

Nomenclature

D_1	Distance between the terminal of servers and the rack rear door, m
D_2	Distance between server and the rack front door, m
D_3	Distance between two rows of rack, m
D_4	Distance between the rear doors of two rack rows, m
L_s	Length of server, m
L_c	Length of air inlet of rack, m
L_r	Length of rack, m
$\vec{u}$	Average velocity vector
p	Static pressure, kPa
T	Static temperature, kPa
$\vec{g}$	Gravitational acceleration vector
v_{eff}	Effective fluid viscosity
k_{eff}	Thermal conductivity
ρ	Air density, kg/m^3
S	Volumetric heat sources,
c_p	Specific heat capacity of air, kJ/ (kg K)
MT_{om}	Exhaust mean air temperature of the optimal model, □
MT_o	Exhaust mean air temperature of the original model, □
SAT_{om}	SAT of the optimal model, □
SAT_o	SAT of the original model, □
Q	Energy, kWh
m	Mass of air, kg
Δt	The SAT difference between the original and optimal model, K
V	The volume of air, m^3
v	Airflow velocity from the air vent, m/s
A	Area of air vent of CRACs, m^2
SAT_{C8-1}	SAT of Case 8-1, □
SAT_{C1}	SAT of Case 1, □

Abbreviation

DC	Data center
HVAC	Heating, ventilation and air conditioning
FNM	Flow Network Method
POD	Proper Orthogonal Decomposition
FB	Flexible baffle
LSTB	Lower-side terminal baffles for server
UFAD	Under-floor air supply
CAC	Cold aisle containment
IR-CA	In-rack cold aisle
OHI	Open hot aisle
CRACs	Computer room air conditioning units
SAT	Supply air temperature
CA	Cold aisle
RANS	Reynolds-averaged Navier-Stokes
VP	Velocity point
RSM	Reynolds Stress Model
DES	Detached Eddy Simulations
MP	Measuring point
RP	Record point
VP	Velocity point
SVP	Simulation velocity point
MS	Ratio of mean temperature to SAT
COP	Coefficient of performance

1. Introduction

Building sectors are responsible for more than 40% of the world's energy consumption and about 30% of the CO_2 emissions [1]. The specific heat load of data center (DC) facilities could be more than 100 times larger than that of a typical similarly sized office building, while the energy use of DCs is 30–50 times that of office buildings [2, 3]. Although DCs are just a small group of building sectors, its energy consumption accounts for about 1.5% of global electricity use, whose figure is especially high in the US at 2.8% [4–6]. Due to the high density and higher heat load of servers, the rising trend in energy use within DCs remains at 20% every year, which also challenges the safe operation of IT equipment [7–9]. IT equipment and cooling systems are two main electricity consumers in DCs, which are responsible for approximate 44% and 40% of total electricity use in a DC, respectively [10]. Cooling systems (e.g. refrigeration compressor and fans) are used to cool overheating IT equipment and keep them operating safely [11, 12]. However, a cooling system requires a lot of energy to guarantee safe operation of DCs [13]. The improvement in cooling efficiency and the balance of cooling energy consumption and safety operation of IT equipment are getting more attention and are worth further study.

According to Khalaj and Halgamuge [14], approaches to improving cooling performance varied from component-level to room-level solutions. Research on the component-level thermal optimization system is rather scant in the DC area [15]. Zimmermann et al. [16] attached micro-channel heat sinks to the electronic boards for heat dissipation from the components. Nie and Joshi [17] did the research on a multiple-scale reduction model by combining the Flow Network Method (FNM) and flux-matching Proper Orthogonal Decomposition (POD) theory to achieve component-level conduction through rack-level convective transport. Compared to the component level, research on the room-level and rack-level high cooling efficiency method has been more popular in the past 20 years. Many researchers have studied the DC room-level methods based on free cooling technologies [18–20] and room-level airflow management, including operating parameters adjustment [21, 22], ventilation configurations [23–26], and aisle containment configuration [23, 27–28]. A free cooling system uses the natural clod sources to cool the DCs in the winter and transitional seasons with lower outdoor temperatures [10]. Wang et al. [18] analyzed the reliability and availability of a hybrid free cooling system with a water-side economizer in a DC, while they also did some uncertainty analysis of supervisory control performance in the same hybrid free cooling system [20]. In addition, Ding et al. [29] experimentally studied the influencing factor of the separated heat pipe system in a DC. There is no doubt that free cooling is a promising energy-saving method applied in a DC, but it is restricted by the limited external conditions in use [30–31]. Thus, free cooling technology cannot be used effectively in all climate zones, while research on

component-level thermal distribution optimization is in its infancy.

Room-level airflow management can improve the overall thermal distribution and reduce energy use, but it cannot solve the problem of thermal environment deterioration of a single rack or local part [13]. Recently, research on the room-level airflow optimization system has tended to be saturated and has come up against a bottleneck, while the rack-level thermal optimization system gets more attention. Almoli et al. [32] attached liquid loop heat exchangers and additional fans on the rack backdoor and found that it can improve the thermal distribution. The results show that the use of heat exchangers at the racks' rear door can improve the thermal environment and reduce cooling energy saving by free cooling. Yuan et al. [15] proposed flexible baffles (FBs) set in the front door of the rack, and they experimentally and numerically investigated the effects of FBs on the airflow distribution in a high-density DC. The results showed that the thermal and airflow distribution is successfully improved in the models with FBs, while the exhaust air temperature drop is proportional to the original temperature and the width of the FBs. Wang et al. [33] proposed an innovative rack-level drawer rack to improve airflow distribution, while the results showed that the hot-air recirculation and cold-air bypass could be significantly improved. Yuan et al. [13] proposed a novel rack-level DC airflow optimization system with lower-side terminal baffles for servers (LSTBs) and concluded that the application of 45° angle and 8 cm × 46-cm LSTBs can alleviate the rack hotspot and improve cooling efficiency. Choi et al. [34] used CFD simulation software to build up a detailed DC model named ThermoStat to study the temperature and airflow distribution in rack-mounted server systems.

The performance of the cooling system can be improved by optimizing rack-level airflow management. The novelty of this paper is to introduce a new concept for the rack-level airflow management where a typical under-floor air supply (UFAD) system with cold aisle containment (CAC) is replaced by an in-rack UFAD system. In this concept, the CAC is converted into a virtue in-rack cold aisle (IR-CA). The study is divided into eight cases with seven different dimensions for the rack air inlet, while an additional partition plane is placed in Case 8 with a 0.6 m × 0.6-m rack air inlet. The simulation results of temperatures and velocities in Case 1 is fully validated by the corresponding on-site experimental results. In this paper, the feasibility of the in-rack UFAD system is validated, and then the impact of different in-rack UFAD systems on the thermal environment optimization in DC is investigated and analyzed. Finally, the energy saving is calculated.

2. Methodology

2.1 Data center description

The studied DC is a typical UFAD DC with CAC and an open hot aisle (OHI), which serves a campus in Nanjing, China, with Internet and communication service. It covers the network demand of approximately 30,000 people. **Fig. 1** shows the studied DC and its layout and plan, while **Table 1** lists the geometry and configuration of the DC. The cool air generated by the computer room air conditioning units (CRACs) supplies the plenum chamber and flows into the CAC through perforated tiles afterwards. The cool air within the CAC is drawn into the rack front door and is exchanged with the hot air at the terminal of servers, and then the mixed air enters the OHI through the rack rear door. Finally, the mixed air in the OHI returns directly to the CRACs. The heat loss of the plenum is assumed to be insignificant.

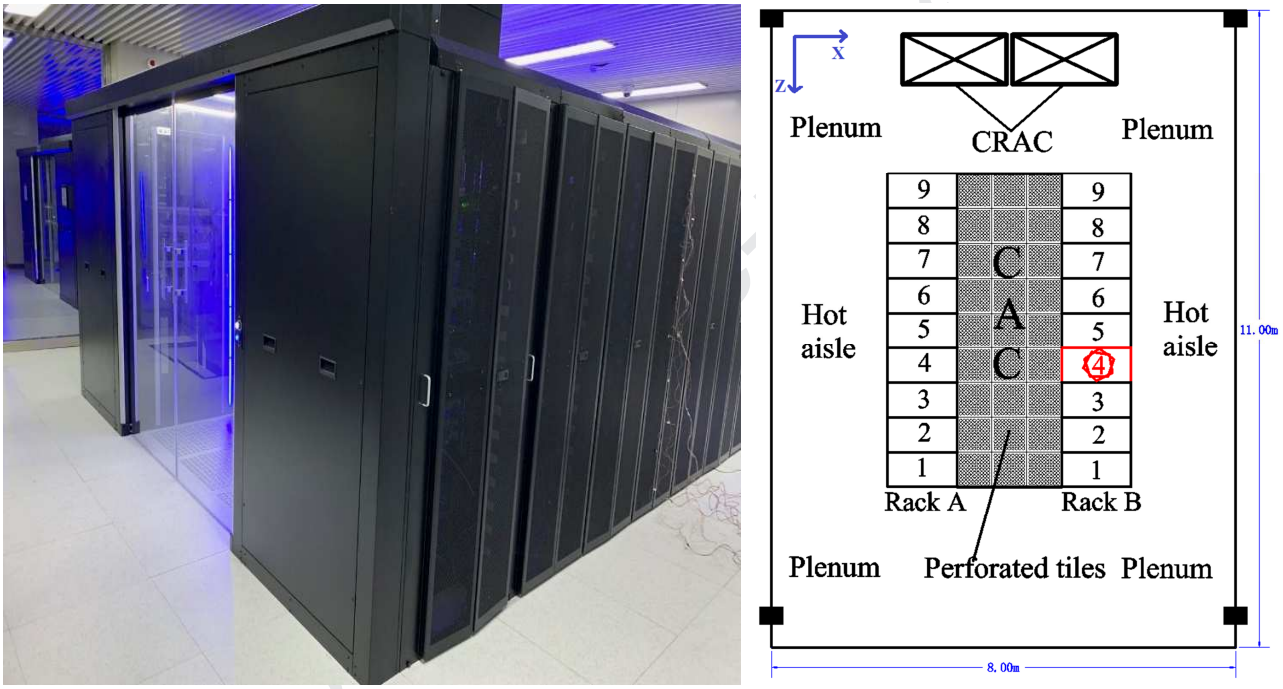

Fig.1. The studied DC (left) and its layout & plan (right).

Table 1

Geometry and configuration of the studied DC

Items	Value
Dimensions of DC	11 m (L) × 8 m (W) × 4 m (H)
Plenum height	0.45 m
Height above the plenum	3.55 m
Plenum	Slightly adiabatic
Air supply mode	UFAD & Direct air return
Aisle configuration mode	1 CAC & 2 OHIs
Dimensions of CACs	5.4 m (L) × 1.8 m (W) × 2.2 m (H)
Number of perforated tiles	Altogether 27 in three rows
Dimensions of perforated tiles	0.6 m (L) × 0.6 m (W)
Porosity of perforated tiles	45%

Room ambient humidity	Below 36%

Two CRACs supply cool air. Their specifications are listed in **Table 2**. The set supply air temperature (SAT) is 22 □, while the actual operating SAT of the two CRACs is 22.2 □ and 22.1 □, respectively. However, the slight deviation of SAT between set and operating SAT is within the acceptable limit. These two CRACs have to work continuously for 24 hrs/day, 365 days/year, while their total power is about 86 kW. This means significant annual electricity consumption at full load. Thus, under the premise of ensuring the safety operation of servers and an acceptable thermal environment in DC, reducing the load of CRACs as much as possible by adjusting its air supply parameters could improve cooling efficiency and minimize energy consumption [15, 21].

Table 2

Specifications of CRACs

Items	Values
Number of CRACs	2
Dimensions of CRACs	1.8 m (L) × 0.8 m (W) × 2.25 m (H)
Distance between CACs and CRACs	1.6 m
Height of CRACs above the plenum	1.8 m
Height of CRACs under the plenum	0.45 m
Dimensions of CRACs' air outlet vent	1.8 m (L) × 0.25 m (W)
Area of each air vent of CRACs	0.45 m^2
Air velocity from the CRACs	5.33 m/s
Set supply air temperature (SAT)	22 □
Operating SAT	22.2 □ & 22.1 □
Total power per CRAC	43.1 kW
Supply air cooling capacity per CRAC	65.8 kW
COP	1.53
Operation time	24/24 hrs, 365 days/year

The racks in the studied DC differ largely from each other; their servers' placement, dimensions, and heat load are different and uneven. **Table 3** shows the geometry and technical description of racks and servers. The rated power varies from 600 W to 4000 W, while the dimensions of the server are also much different. For this study, Rack B4 is selected as the studied rack for the following reasons: 1. All the servers have the same dimensions; 2. The servers have only two rated powers (495 W× 2 and 750 W × 2); 3. Relatively even spacing between servers; 4. The highest rated power of 16.98 kW.

Table 3

Geometry and technical description of racks and servers

Items	Values
Number of racks	Altogether 18 in 2 rows (Rack A & Rack B)
Dimensions of each rack	1.2 m (L) × 0.6 m (W) × 2.2 m (H)

Front door porosity	65%	
Rear door porosity	65%	
Rated power of racks	Varied between 0 kW and 16.98 kW	
Dimensions of servers	0.8 m (L) × 0.46 m (W) × 0.09 m (H)	
	0.7 m (L) × 0.46 m (W) × 0.09 m (H)	
	0.8 m (L) × 0.46 m (W) × 0.045 m (H)	
	0.8 m (L) × 0.46 m (W) × 0.18 m (H)	
Rated power of servers	300 W × 2	495 W × 2
	600 W × 2	750 W × 2
	900 W × 2	2000 W × 2
Dimensions of servers in studied rack	0.8 m (L) × 0.46 m (W) × 0.09 m (H)	
Rated power of servers in studied rack	(495 W× 2) × 2	(750 W × 2) × 10
Distance between neighboring servers	0.09 m	0.045 m

2.2 On-site experimental description

The simulation model is validated by on-site experiments carried out in September 2018 at a university in Nanjing, China. **Fig. 2** shows the temperature measuring points (MPs) in the experiments and the configuration of these points, while **Table 4** shows the experimental equipment information. The measured object is Rack B4, while seven MPs were temperature sensors set at the rear door of the rack. The temperature sensors are linked to the data acquisition logger, while the temperatures from the sensors will be recorded by the logger, and then transmitted to the personal computer. The measurement period lasted approximate 2 h. The supply air temperature and velocity of CRACs are measured by the handheld airflow anemometer of model number 'KIMO VT200/FC300'. The measured air temperature was 22.1 □, and the air velocity was 5.33 m/s in the middle area of the air vent of CRACs.

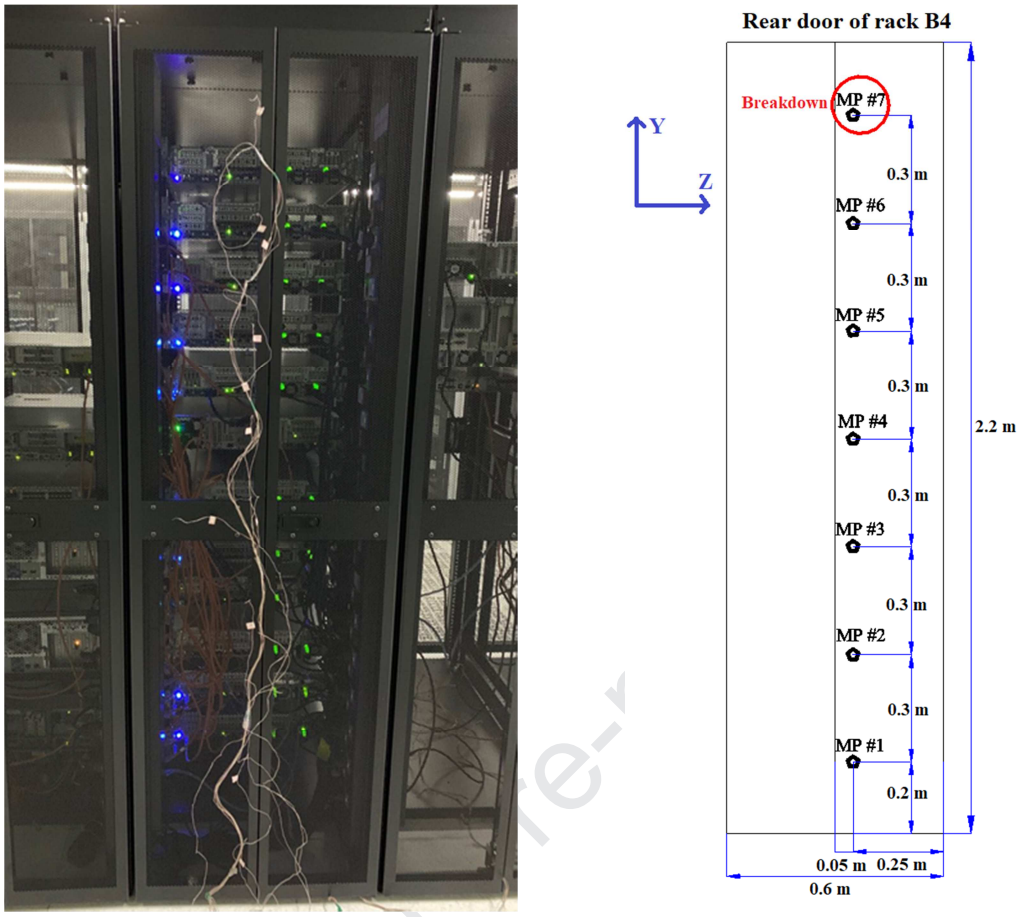

a) b)

Fig. 2. The temperature measuring points setup. a) Temperature measuring points in the measurements; b) The configuration of these points.

Table 4

Experimental equipment

Experimental equipment	Model	Measuring range	Accuracy
Temperature sensor	Type K thermocouples of nickel chromium-silicon	-20 □~400 □	±0.4%
Data acquisition logger	Aglient 34972A	N/A	N/A
Handheld airflow anemometer	KIMO VT200/FC300	Temperature: -20 □~80 □ Velocity:0.15~30 m/s	±0.4% ±2%

Consistent with the MPs in the experiments, the corresponding record points (RPs) in the simulation are used to compare the experimental and simulation results. The positions of RPs are the same as the MPs shown in **Fig. 2b**. However, the temperature sensor in the MP 7 is broken in the experimental process; therefore, the data of MP 7 is excluded. According to Yuan et al. [13] and Yuan et al. [15], 6 temperature measuring points are enough to express exhaust air temperature distribution and validate the accuracy of simulation. In addition, the temperature in the MP 7 is relatively low, which cannot be the rack hotspot. Thus, the exclusion of MP 7 has little effect on the determination

rack hotspot and validation. Expect of temperature MPs, the velocities of the servers' terminal are also measured by the handheld airflow anemometer. The positions of the velocity points (VPs) in the measurement are shown in **Fig. 3**, while the corresponding velocity record points in the simulation are named as simulation velocity points (SVPs). In addition, **Fig. 3** also shows the detailed rated powers of each server.

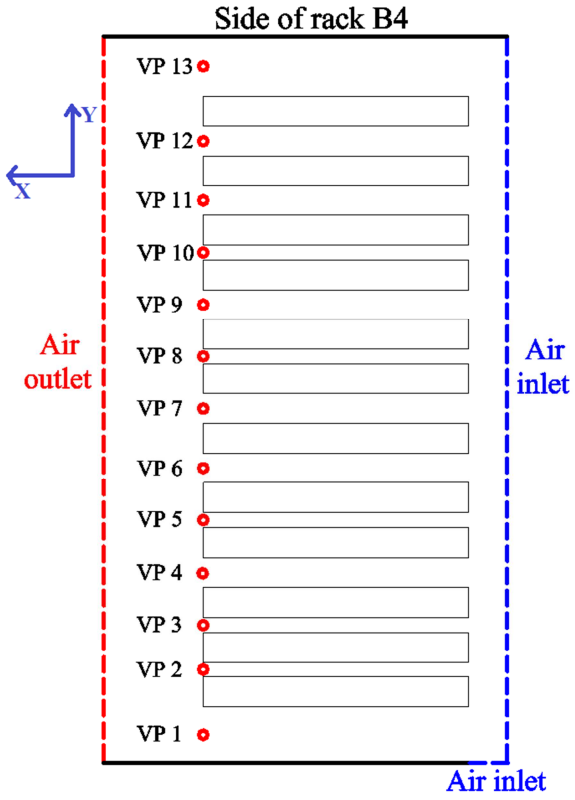

Fig. 3. The positions of the velocity points (VPs) in the measurement.

2.3 Numerical simulation description

Refer to the geometry and specifications in **Tables 1–3**. A DC model is constructed using the commercial CFD software Airpak 3.0 for numerical investigation. **Fig. 4** shows the CFD model of the studied DC. A trial simulation was done in the model with all the parameters of racks and servers consistent with the actual DC. The mesh number reached the 28,000,000^{+} level, while the convergence time for the trial simulation took more than 7 hours. Thus, the model was simplified to save simulation time. In the following numerical simulations, only racks B3-5 were equipped with servers based on the actual servers' status, while other racks are empty of servers for the simplification of the simulation model. The simulation results of Rack B4 before and after simplification were almost identical [13, 15]. The simplified model is applied in all the cases described in **Table 5**. **Table 5** shows the specific case description including cold aisle (CA) mode and geometry dimensions. Case 1 adapts a CAC, while cases 2–7 replaces the CAC by IR-CA. In cases 2–7, the only independent variable is D_2 and L_c, and except in Case 1, D_2, and L_c are the same

parameter in cases 2–7. The value of D_1, L_s, and D_3 are the same in cases 2–7, respectively. D_1 represents the distance between the terminal of servers and the rack rear door, while D_2 is the distance between the server and the rack's front door. In addition, D_3 is the distance between two rows of racks, and D_4 represents the distance between the rear doors of two rack rows. The air supply parameters of the CRACs in cases 1–8 are the same.

The layout and specification of Rack B4 in seven cases can be seen in **Table 5** and **Fig. 5**. The schematic map of these cases in **Fig. 5** is based on the central section of Rack A4, cold aisle, and Rack B4 in **Fig. 4**. The red dotted lines and blue solid lines in **Fig. 5** represent the rack air outlet and inlet, respectively.

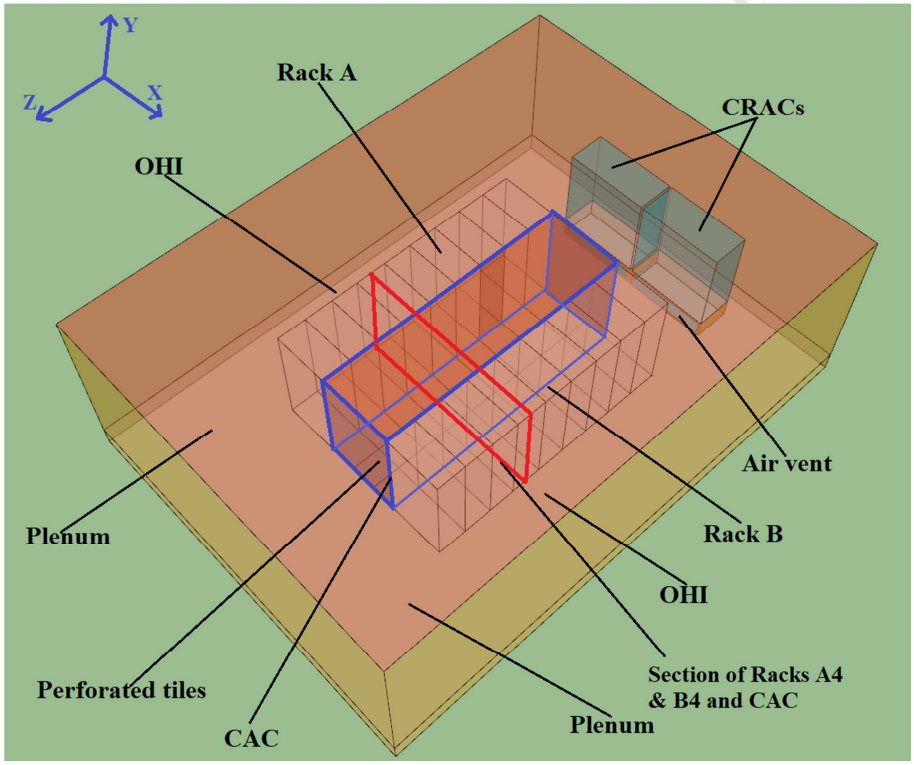

Fig. 4. Schematic diagram of CFD model of the studied DC.

Table 5

Case categories and descriptions

Case	1	2	3	4	5	6	7	Remarks
CA mode	CAC	IR-CA	IR-CA	IR-CA	IR-CA	IR-CA	IR-CA	N/A
D_1 /m	Constant value：0.3							N/A
L_s /m	Constant value：0.8							N/A
D_2 /m	0.1	0.2	0.3	0.4	0.5	0.6	0.7	N/A
L_c /m	2.2	0.2	0.3	0.4	0.5	0.6	0.7	N/A
D_3 /m	1.8	Constant value：0.6						N/A
L_r /m	1.2	1.3	1.4	1.5	1.6	1.7	1.8	$L_r=D_1+L_s+D_2$
D_4 /m	4.2	3.2	3.4	3.6	3.8	4	4.2	$D_4=L_r+D_3$

D_1 is the distance between the terminal of servers and the rack rear door. D_2 is the distance between server and the rack front door. D_3 is the distance between two rack rows. D_4 is the distance between the rear doors of two rack rows. L_s is the length of the server. L_c is the length of a rack's air inlet. L_r is the rack's length.

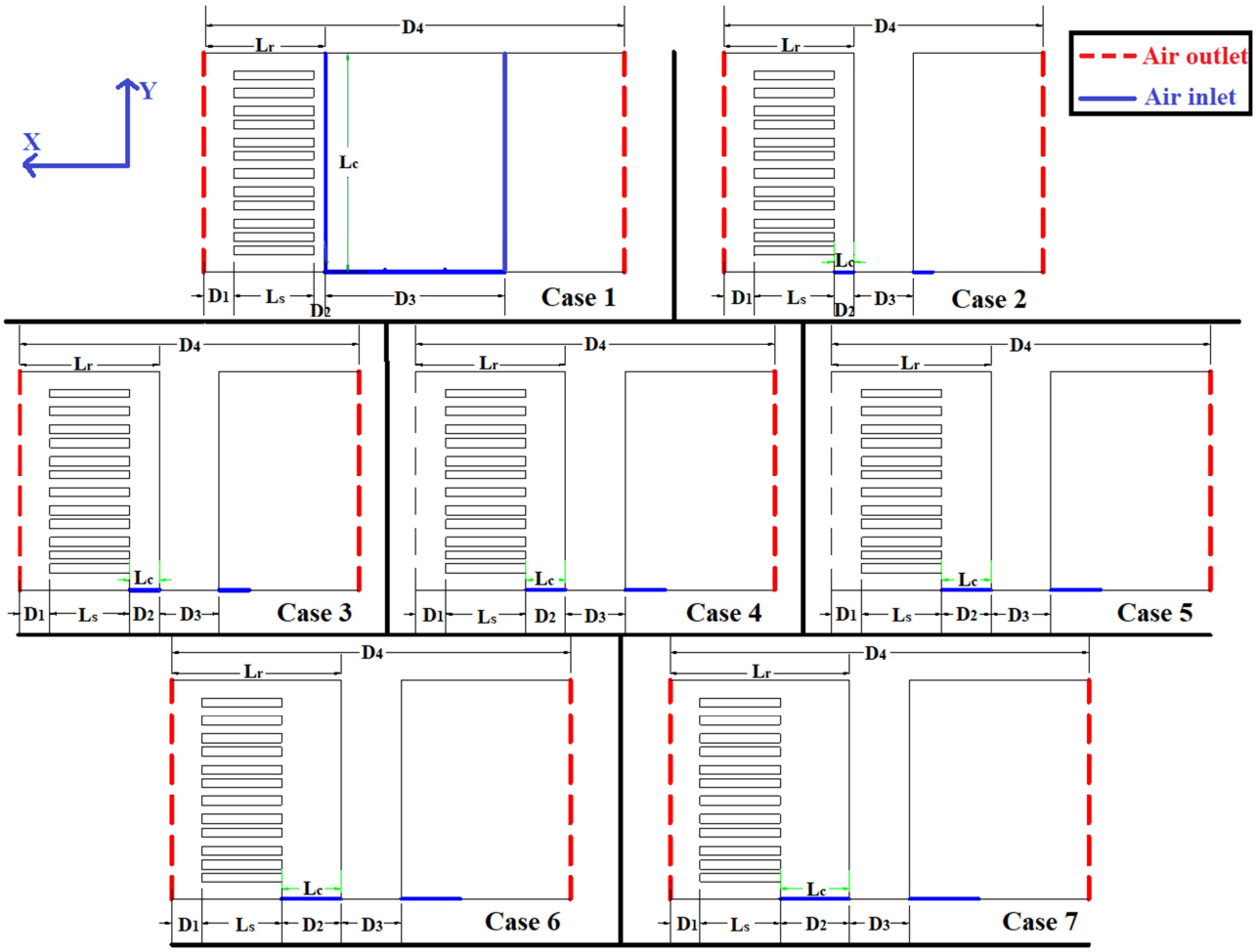

Fig. 5. The size and location of rack air inlet in seven cases.

The flow regime of the simulation models is turbulent mixed convection in consideration of the airflow conditions, scales of racks, and server in DC. Phan et al. [35] applied and compared server Reynolds-averaged Navier-Stokes (RANS) turbulent models in DC in terms of simulation time and accuracy. They found that the zero-equation model performs better than standard the k–ε model in consideration of well-balanced and time-targeting models. In addition, Wibron et al. [36] recommended that the RSM model performed better than DES and the *k–ε* model for precise simulation results. However, the simulation results in the zero-equation model is not as precise as that in the standard k–ε model, while the RSM model takes 15–20% more memory and has a longer convergence time than the standard *k–ε* model [37, 38]. In addition, the standard k–ε model has been applied in many DC researches, while research on the application of the zero-equation and RSM models in DC are relatively few [13, 15, 39–43]. **Fig. 6** shows the comparison of temperature

distributions between the experimental results and simulation results in different turbulent models. The RSM turbulent model ranks first in terms of deviation between experimental results and simulation results, followed by the standard k–ε model, while the accuracy of the zero-equation model is the worst among them. However, the accuracy difference between the RSM model and standard k–ε model is slight, and the RSM model takes 1.8 times the convergence time compared with the standard *k–ε* model for each case. Thus, comprehensively considering the application scope, accuracy, CPU utilization percentage, and convergence time, the standard *k–ε* turbulent model is applied in this paper. As shown in **Table 6**, there are also some assumptions in the simulation process with the standard *k–ε* turbulent model, while the momentum, continuity, and energy conservation equations for the impressible fluid are also listed in **Table 7.**

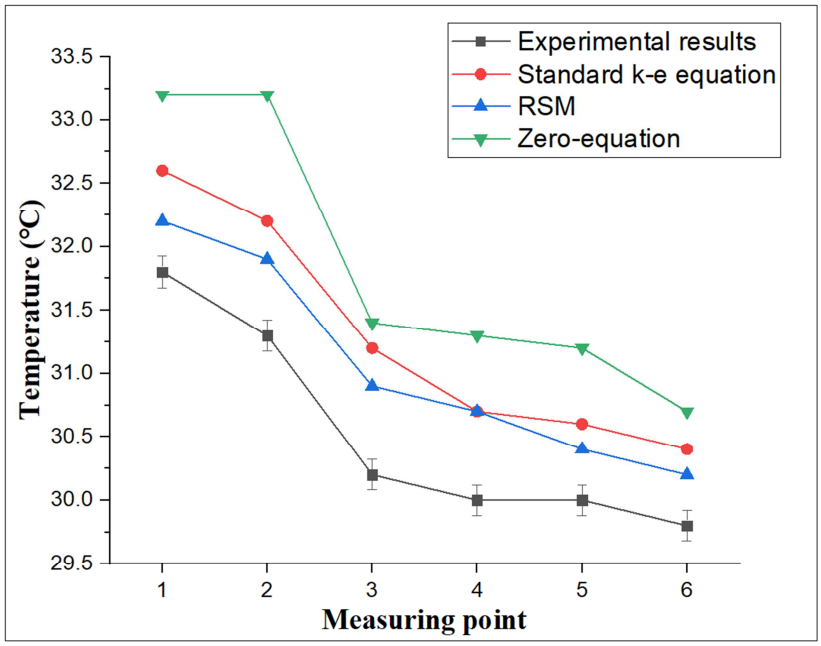

Fig. 6. The comparison of temperature distributions between the experimental results and simulation results in different turbulent models.

Table 6

Simulation assumptions and governing equations

Items		Description
Assumptions: [13, 44–46]		
		No radiation effects No air leakage Incompressible fluid used The same supply air temperature in all tiles
Governing equations:		
Continuity	**Equation 1**	$\nabla \cdot \vec{u} = 0$
Momentum	**Equation 2**	$\frac{\partial \vec{u}}{\partial t} + \vec{u} \cdot \nabla \vec{u} = \nabla \cdot \left(v_{eff} \nabla \vec{u}\right) - \frac{1}{\rho} \nabla p + \vec{g}$

Energy conservation	**Equation 3**	$\rho c_p \left[\frac{\partial T}{\partial t} + (\vec{u} \cdot \nabla)T\right] = \nabla \cdot \left(k_{eff} \nabla T\right) + S$

Table 7

Simulation discretization solution and parameter settings

Items	Variables	Value	Remarks
CRACs	Airflow velocities	5.33 m/s	2 CRACs
	SAT	22 □	N/A
Discretization solution [47]	Discretization scheme	Second-order upward	
	Under-relaxation	0.3	For all temperature, momentum, and pressure
	Solving format	AMG	
	Type of linear solver	Flex	
Convergence criteria [15]	X, Y, and Z direction	1×10^{-3}	
	Continuity	1×10^{-3}	N/A
	Energy	1×10^{-6}	
	Dissipation rate	1×10^{-3}	
Mesh parameters [13, 15]	Mesh type	Hexa unstructured	N/A
	Grid generation criteria	Variable-based smooth element & density changes	N/A
	Mesh quality	1	More than 95%
	Face alignment	Larger than 0.15	No element severely distorted
	Mesh spacing	Non-uniform	In the overall domain
	Spacing between grid points	From 0.015m to 0.035m	N/A

Table 7 summarizes the convergence criteria, discretization solution, and other simulation parameters. Mesh number plays an important role in the simulation period, affecting the simulation time and accuracy and even directly deciding on the success or failure of the simulation [47]. A coarse grid can contribute to numerical errors, while significant increases in mesh number can cause round-off errors. Thus, a proper grid number can reduce both the numerical errors and round-off errors [13]. The grid independence test should be done to check the grid quality, while different grid numbers are chosen to find the proper grid number. The grid independence test applied in this paper has been used in many open literatures and is regarded as an appropriate method [13, 15, 49–51]. **Fig. 7** shows the grid independent test of Case 1. When the mesh number is larger than 1,802,216, the maximum exhaust air temperature of Rack B4 remains steady. Thus, the mesh number of 1,802,216 is chosen as the proper grid number, while the mesh quality is checked as qualified by the self-contained Grid Quality Inspection Tool of Airpak3.0. In addition, no element has been distorted, as the calculation of face alignment was larger than 0.15.

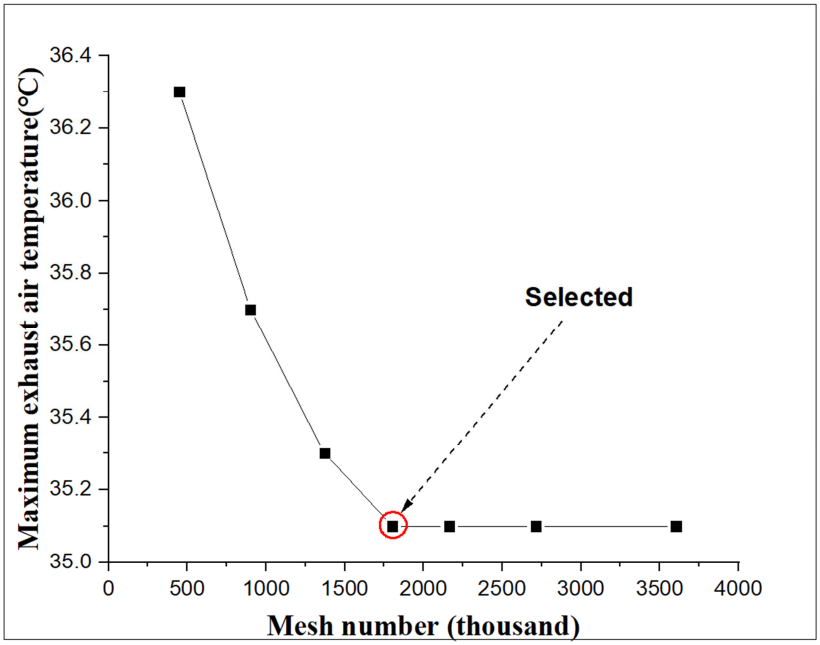

Fig. 7. The variations of maximum exhaust air temperature of Rack B4 with grid number in Case 1

2.4 Validation experiments

Fig. 8 shows the temperature validation between experimental results and simulation results in Case 1. The temperature trend of the points in the experiment and simulation are almost the same, while the simulated values are slightly larger than the measured values in all the MPs/RPs. In addition, the maximum deviation of the temperatures between corresponding MPs and RPs is smaller than 3.5%. Thus, the numerical results are consistent with the experimental results in terms of the temperature of the MPs/RPs. Likewise, as shown in **Fig. 9**, the velocity trend of the points in the experiment and simulation are the almost same, while the maximum deviation of the velocities between corresponding VPs and SVPs is smaller than 11.5%. Thus, the numerical results are consistent with the experimental results in terms of the velocities of the VPs/SVPs. In summary, the simulation model is strongly validated by the experimental results in terms of temperature and velocity. **Fig. 9** can also explain why the exhaust temperatures of six measuring points in the experiment are higher than the corresponding temperatures in the numerical results in **Fig. 8**. The larger velocities result in lower temperature distribution.

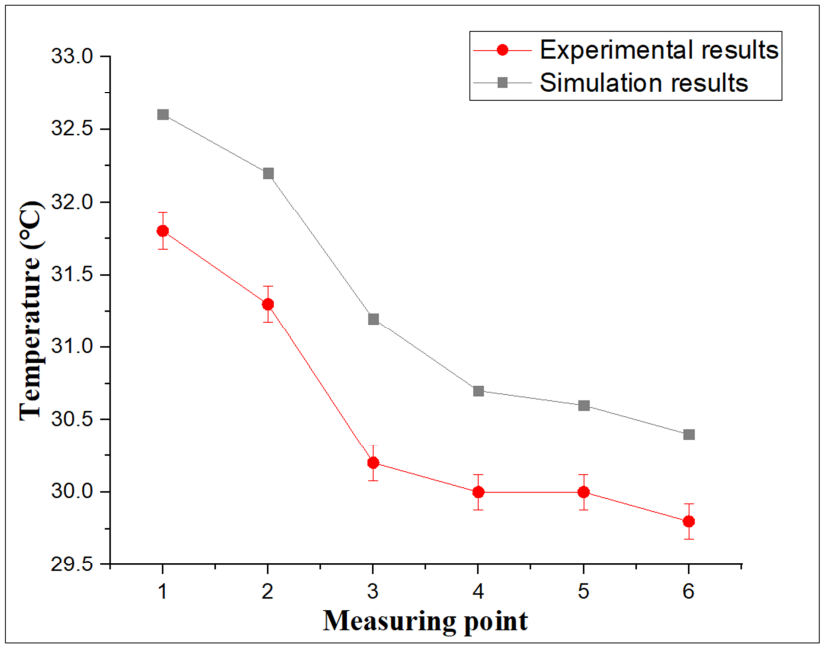

Fig. 8. Temperature validation between experimental results and simulation results in Case 1.

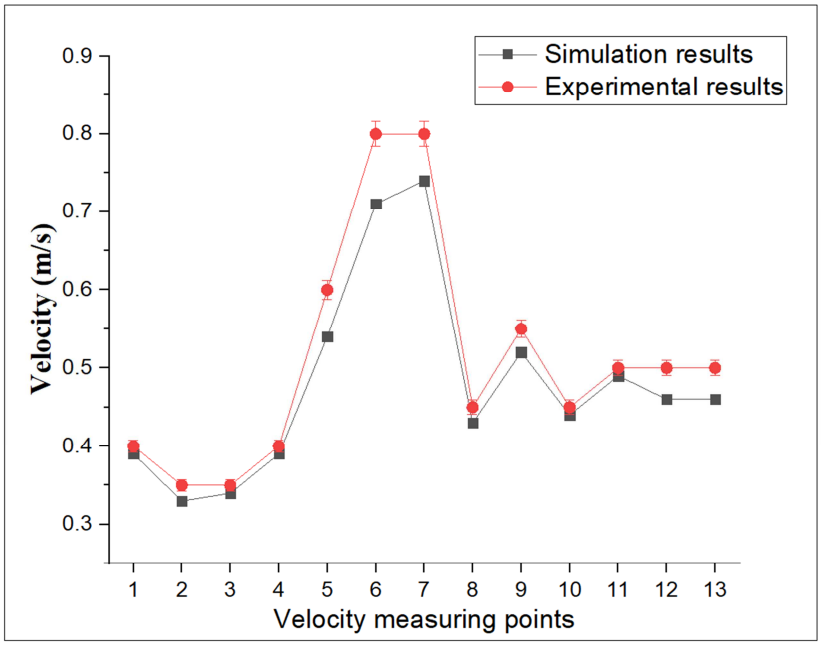

Fig. 9. Velocity validation between experimental results and simulation results in Case 1.

3. Temperature and airflow distribution analysis

The study is divided into eight cases with seven different dimensions of rack air inlet (2.2 m × 0.6 m, 0.2 m × 0.6 m, 0.3 m × 0.6 m, 0.4 m × 0.6 m, 0.5 m × 0.6 m, 0.6 m × 0.6 m, and 0.7 m × 0.6 m), while an additional partition plane is placed in Case 8 with a 0.6 m × 0.6 m rack air inlet. The temperature and airflow distributions in cases 1–7 are obtained and analyzed, and then the impacts of

IR-CA on the thermal environment were analyzed and discussed.

3.1 Optimization of temperature distribution

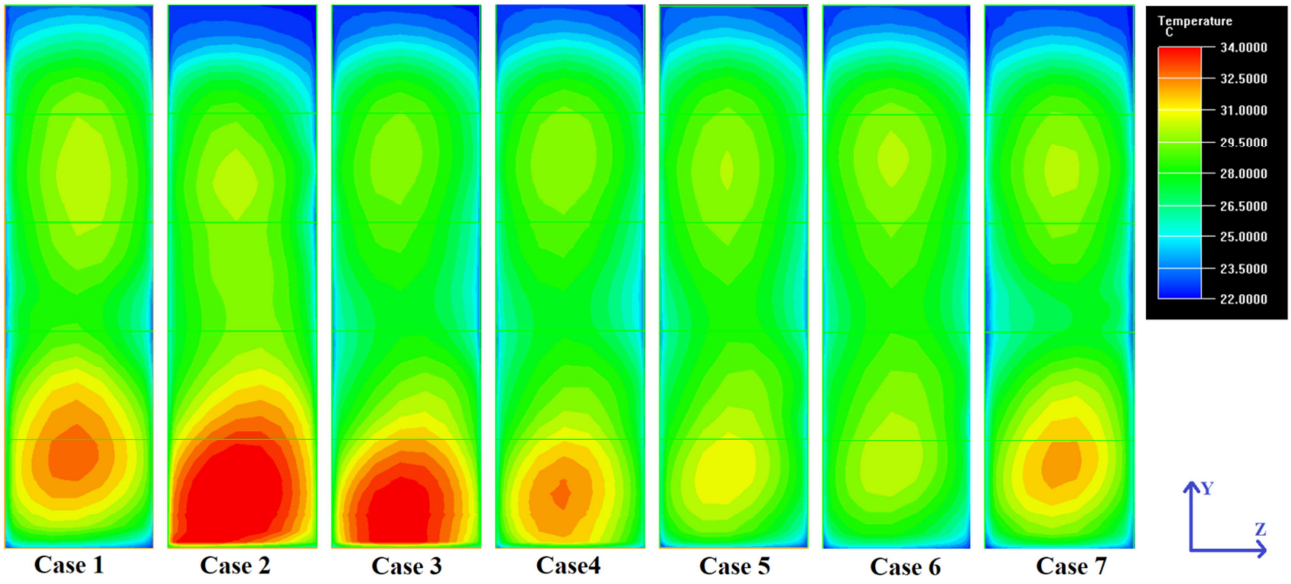

Fig. 10. Exhaust air temperature profiles of Rack B4 in seven cases.

Fig. 10 shows the exhaust air temperature distribution of Rack B4 in seven cases. In Case 1, the cool air is supplied through the front door of Rack B4 from the UFAD system with CAC, while the cool air is directly drawn into the rack through the under-floor perforated tiles within the rack in cases 2–7. Compared to Case 1, the CAC is replaced by a virtual IR-CA in cases 2–7. As shown in **Fig. 10**, an obvious heat accumulation exists in the lower part of Rack B4 in Case 1. The application of IR-CA can to varying degrees improve the exhaust air distribution of the middle and top part of Rack B4 in all cases 2–7. For the lower part of Rack B4, the heat accumulation phenomenon in cases 2 and 3 gets worse, which means that the application of IR-CA in cases 2 and 3 cannot improve the airflow and thermal distribution of B4. However, when the width of IC-RA increases from 0.4 m in Case 4 to 0.6 m in Case 6, the heat accumulation in the lower part of Rack B4 is significantly reduced, while the heat is never accumulated in the lower part in Case 6. When the width of IR-CA increases to 0.7 m, the heat accumulation phenomenon recovers in the lower part of Rack B4. Thus, combining the optimization effects of the whole rack, Case 6 performed best in terms of heat accumulation mitigation and temperature distribution uniformity.

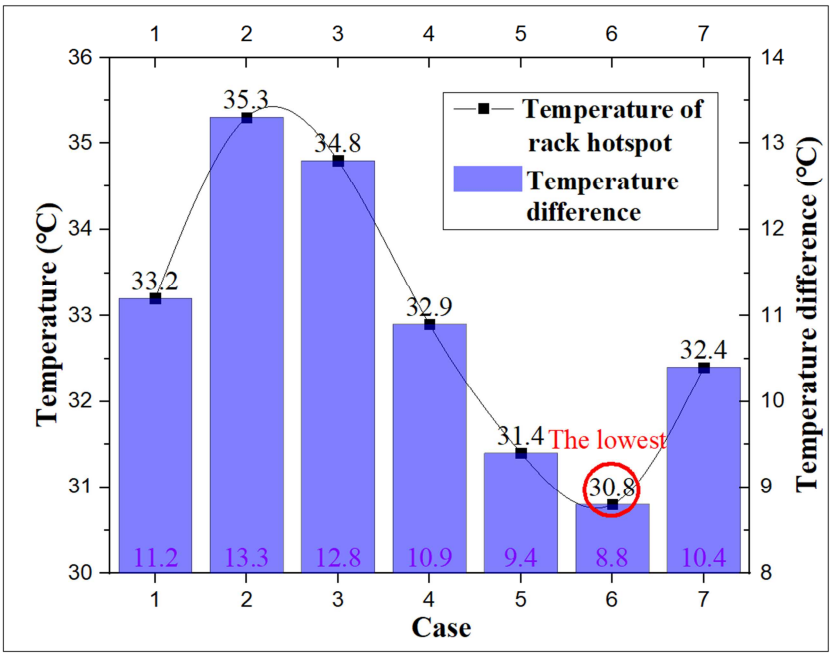

Fig. 11. Temperature variation of rack hotspot and maximum temperature difference in seven cases.

According to Yuan et al. [13], the rack hotspot was defined as the point where the maximum exhaust temperature of each rack is located. The rack hotspot can reflect the uniformity of the exhaust temperature of the racks. **Fig. 11** illustrates the temperature variation of the rack hotspot and maximum temperature difference in seven cases. The temperature of the rack hotspot stands at 33.2 □ in Case 1 and then rapidly increases to up to 35.3 □ in Case 2, where there is an exponential decrease to an all-time low of 30.8 □ in Case 6. In Case 7, the rack hotspot temperature recovers to 32.4 □. Thus, the rack hotspot of Rack B4 reaches the minimum in Case 6. Likewise, the maximum exhaust air temperature difference of Rack B4 shares the same change trend with the rack hotspot, while the maximum exhaust air temperature difference is the lowest at 8.8 □ in Case 6. Thus, Case 6 can achieve the lowest rack hotspot and maximum temperature difference.

In **Fig. 12**, the purple bar represents the temperatures of six RPs in Case 1, while the lines represent the temperature of six RPs in cases 2–7. As shown in **Fig. 12**, there are always some points in cases 2–4 where the temperatures are higher than the corresponding points in Case 1. However, the temperature of all RPs in cases 5–7 is lower than the corresponding points in Case 1. In addition, compared to cases 5–7, the temperature range of six RPs in Case 6 is relatively smaller, which is concentrated in Zone 1 (from around 29.5 □ to about 30.5 □). Therefore, the temperature of RPs is the most uniform in Case 6.

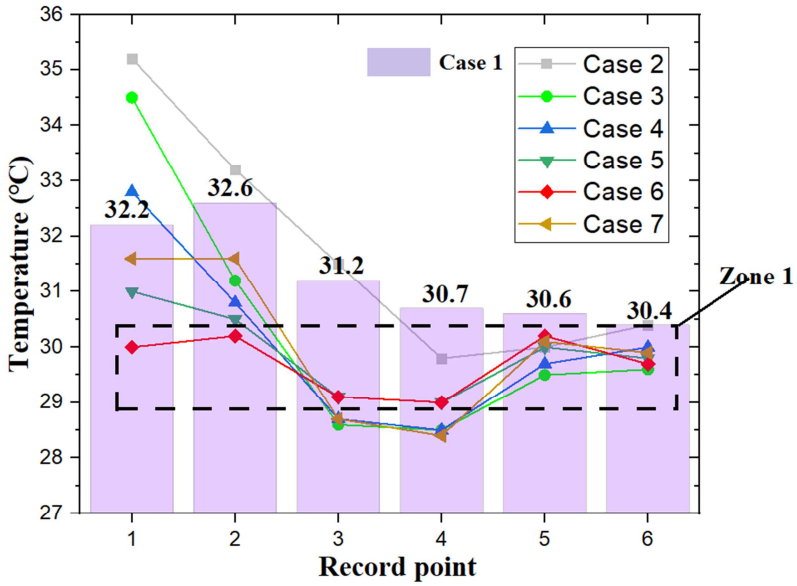

Fig. 12. The temperature variation of six RPs in seven cases

To sum up, when the width of IR-CA is larger than 0.3 m, the in-rack UFAD system can improve the thermal distribution of Rack B4. In addition, concerning the heat accumulation mitigation, exhaust air temperature distribution, rack hotspot, maximum temperature difference, and uniformity of RPs' temperature, the optimal thermal distribution can be obtained in Case 6 with 0.6 m IR-CA in width. The maximum temperature drop in the rack hotspot can reach 2.4 K.

3.2 Airflow velocity optimization

Fig. 13 shows the airflow within the rack in Case 1. The airflow velocities in different parts of servers are quite different in height. In **Fig. 13**, air velocities are divided into four zones. The velocities in Zone 2 rank first, which is followed by those in Zone 3. Next come the velocities in Zone 4, while Zone 1 has the lowest airflow velocities among all four zones. As the analysis in **Fig. 10** shows, heat is heavily accumulated in the lower part of Rack B4, while there is also a slight heat accumulation in the top part of the rack. Thus, the lowest airflow velocity in the lower part of the racks contributed to the heat accumulation in this part, while the relatively lower airflow velocity led to another slight heat accumulation in the top part.

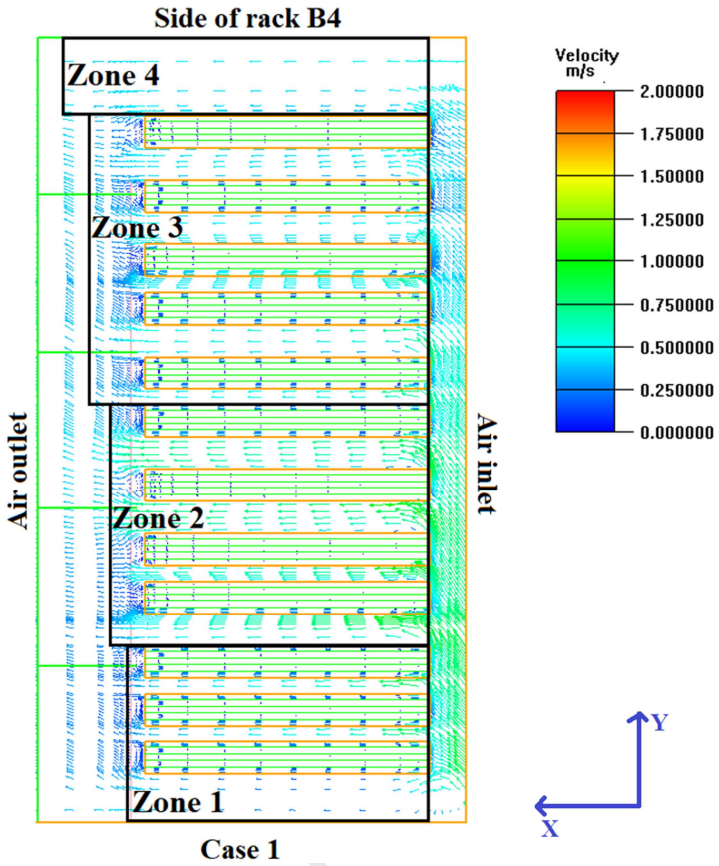

Fig. 13. The airflow within the rack in Case 1 (side view).

However, as shown in **Fig. 14,** the non-uniform airflow distribution is improved to varying degrees in the application of in-rack UFAD systems. **Fig.14** explains the principle of the in-rack UFAD system by analyzing the velocity map of the side of Rack B4, while it shows the airflow velocities within Rack B4 in seven cases. In Case 1, the velocity of the air inlet is very slow, while the air velocity through the air inlet has been greatly increased in all cases 2–7. The velocities in the lower part of Rack B4 is improved the most in Case 6, successfully alleviating the temperature accumulation in the lower part of Rack B4. In addition, the velocity distribution becomes more uniform at the terminal of the servers. Thus, Case 6 performs the best in terms of the velocity improvement in the lower part of Rack B4 and overall velocity distribution uniformity.

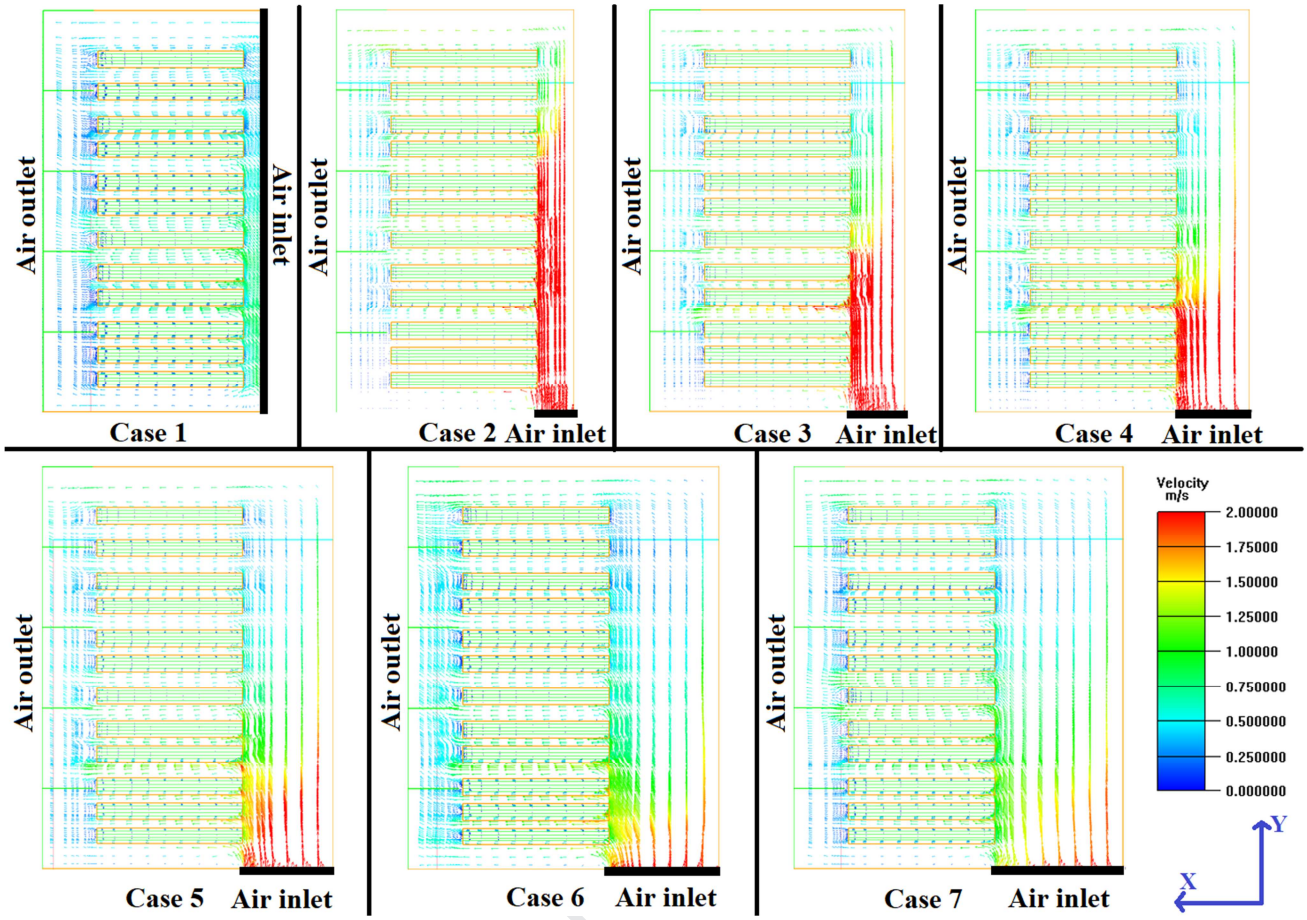

Fig. 14. Airflow velocities within Rack B4 in different cases

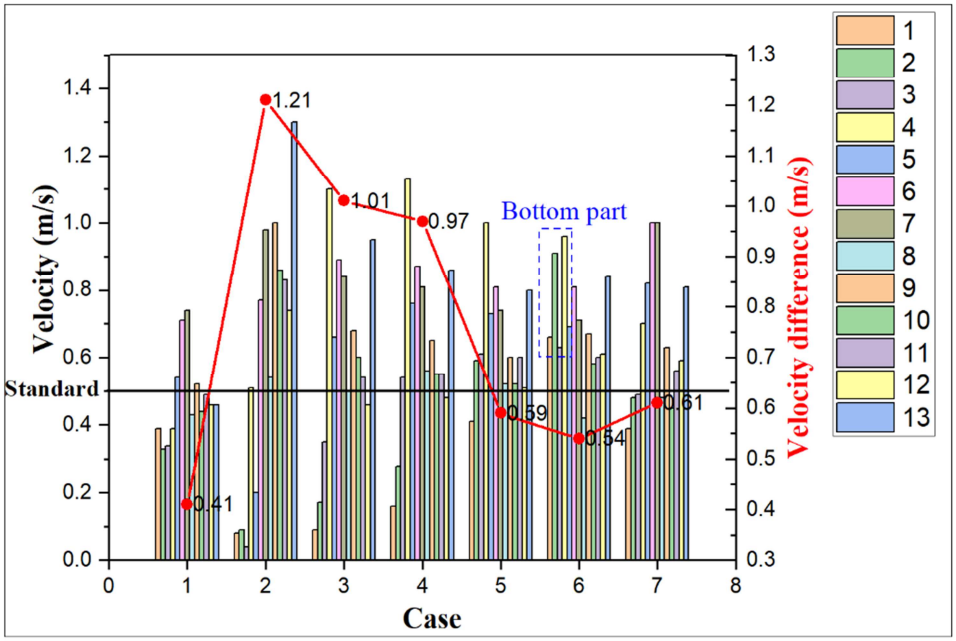

Fig. 15. The air velocity profiles of thirteen VPs and maximum velocity difference in seven cases.

Fig. 15 shows the air velocity profiles of thirteen SVPs and the maximum velocity difference in seven cases: the larger the velocity difference, the less uniform supply air in the upper and lower part

of the rack. The maximum velocity difference of thirteen VPs is the lowest at 0.41 m/s in Case 1, while those in cases 5–7 the difference is 0.54–0.61 m/s. However, the maximum velocity differences become too large in cases 2–4, whose figures are 0.97, 1.01, and 1.21 m/s, respectively. Thus, Case 1 ranks first in terms of supply air uniformity, which is followed by Case 6, then Case 5 and Case 7.

The bar graph in **Fig. 15** shows the air velocities at thirteen SVPs in seven cases. The majority of velocities of SVPs are relatively low, which are below 0.5 m/s in Case 1, while the velocities of most SVPs are greater than 0.5 m/s in cases 2–7. There is only one SVP whose velocity is below 0.5 m/s in cases 5–6, while the number of VPs with a velocity below 0.5 m/s is at least three in the other cases. Thus, cases 5–6 have a relatively uniform air supply when there is a higher mean air velocity level. As shown in **Fig. 10** and **Fig. 13,** heat accumulation exists in the lower part of Rack B4, while the supply of cool air in Zone 1 is insufficient. The greater supply air velocity of a rack's bottom part, the better airflow and temperature distribution. As shown in **Fig. 15**, the air velocities of a rack's bottom part in Case 6 are greater than those in Case 5. Thus, Case 6 performs the best in terms of high supply air velocity level and heat accumulation mitigation in the bottom part of Rack B4. Case 6 can achieve three optimizations at the same time: supply air uniformity, higher supply air velocity level, and heat accumulation mitigation.

To sum up, combining the analysis of both temperature and velocity distribution optimization in cases 1–7, 0.6 m × 0.6 m IR-CA in Case 6 can achieve the optimal thermal distribution and supply air uniformity and relieve the heat accumulation.

4. Advanced model analysis

Although Case 6 improves the airflow and thermal distribution of Rack B4 to a great extent, the airflow through the route between the upper side of the top server and rack top surface has a relatively high velocity compared to some other tunnels between neighboring servers in Rack B4, while the majority of the cold air bypassed and flowed directly out of the rack, causing the waste of cold air. Thus, an additional Partition plane is placed horizontally between the upper side of the top server and the rack front door in Case 8. The side description and the 3-D model of Rack B4 in Case 8 are shown in in **Fig. 16**. The dimension of the partition planes is 60 cm × 60 cm × 0.1 cm.

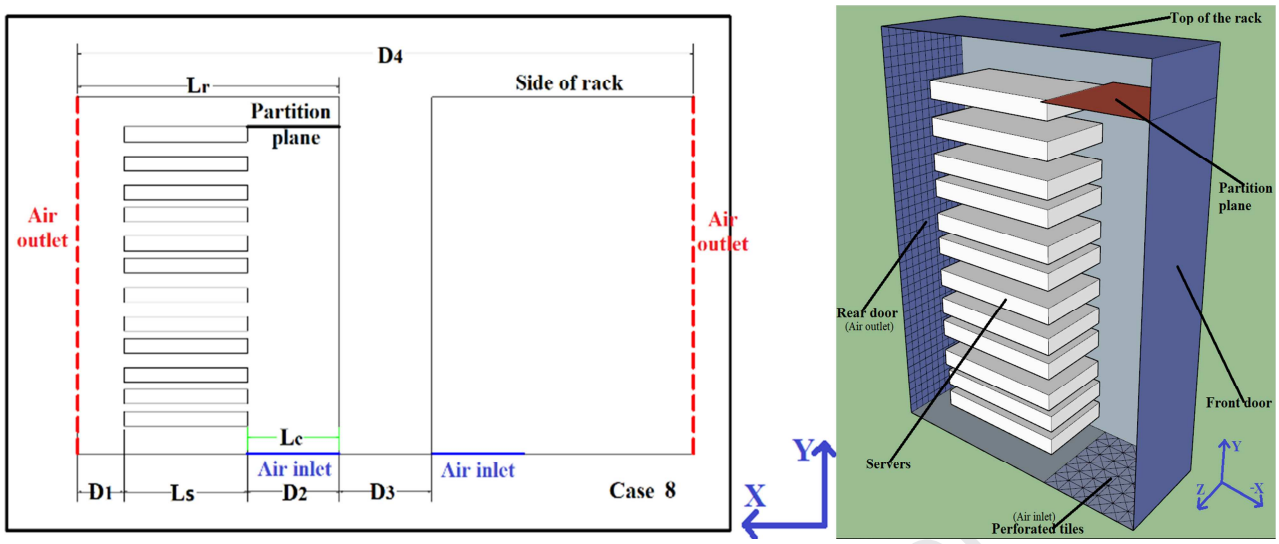

Fig. 16. The side description (left) and 3-D model (right) of Rack B4 in Case 8.

4.1 Temperature and airflow analysis

Fig. 17 shows the exhaust air temperature and airflow distribution of Rack B4 in cases 1, 6, and 8. The lower airflow velocity contributed to higher exhaust air temperature in the same horizontal plane. Compared to Case 1, the heat accumulation is reduced significantly in both cases 6 and 8, while the exhaust air temperature distribution is obviously improved. In addition, the velocities of rack lower part are greatly enhanced in both cases 6 and 8. However, the application of a partition plane in Case 8 prevents the cold air escaping through the gap of the upper server side. As shown in Fig. 16, compared to Case 6 with Case 8, the airflow velocities of the middle and top part of Rack B4 are increased. The air velocities are the most uniform in Case 8. Thus, compared to Case 6, the heat accumulation in the top part is further mitigated in Case 8, while the heat accumulation in the lower part is almost the same.

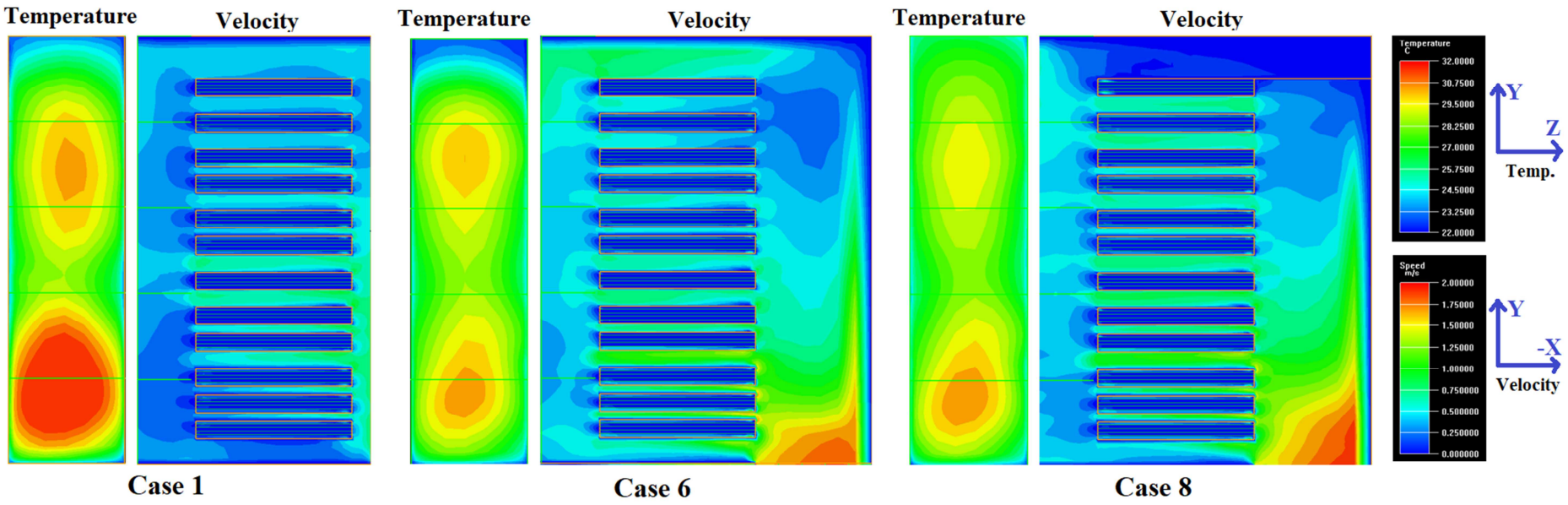

Fig. 17. The exhaust air temperature distribution and airflow distribution of Rack B4 in cases 1, 6, and 8.

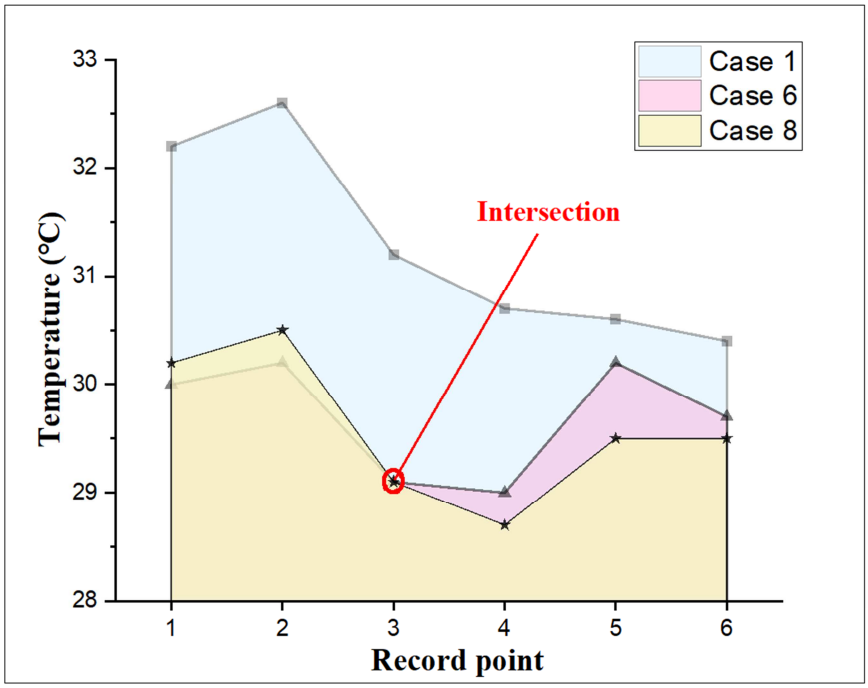

Fig. 18. The exhaust air temperature of six RPs in cases 1, 6, and 8.

In addition, the temperatures and velocities of the corresponding RPs and SVPs in cases 6 and 8 are shown in **Fig. 18** and **Fig. 19**, respectively. As shown in **Fig. 18,** the temperatures of all the RPs in cases 6 and 8 are much lower than the corresponding points in Case 1. The temperatures of six RPs in cases 6 and 8 are divided by the third RP. In RPs 1 and 2, the temperature in Case 8 is slightly higher than that in Case 6, while the temperature in RP 3 is the same in cases 6 and 8. In VPs 4–6, Case 8 has obviously lower temperatures than Case 6. Thus, considering the temperature of all RPs synthetically, Case 8 improves the temperatures of RPs more than Case 6. The corresponding analysis of velocity distributions in cases 6 and 8 is shown in **Fig. 19**. Except for SVP 8 in Case 6 and SVP 13 in Case 8, the velocities of all the VPs are higher than the corresponding VPs' velocities in Case 1. Thus, both cases 6 and 8 have a higher air velocity in Rack B4 than Case 1. However, Case 6 has slightly higher velocities in SVPs 1–3, while Case 8 has higher velocities than Case 6 in SVPs 4–12 to varying degrees.

Through comparing and analyzing the temperature and airflow distribution of cases 1, 6, and 8, it can be concluded that the airflow and temperature distribution in Case 8 is more uniform than that in Case 6.

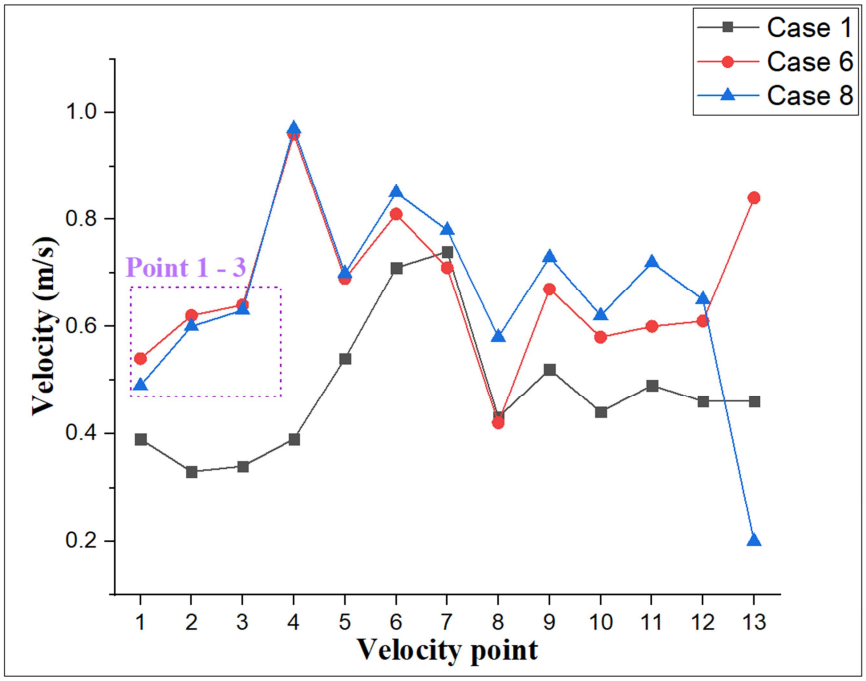

Fig. 19. Airflow velocities of thirteen VPs in cases 1, 6, and 8.

4.2 Energy saving

Based on the thermal distribution analysis, the application of a 0.6 cm × 0.6 m IR-CA and 0.6 m × 0.6 m × 0.1-m partition plane in Case 8 can achieve optimal thermal distribution and minimize the rack hotspot. In order to calculate the energy-saving potential of Case 8 compared to Case 1, the SAT of CRACs is adjusted to 23 □ and 23.5 □ to simulate the temperature and airflow distribution. Case 8 with SATs of 23 □ and 23.5 □ are named cases 8-1 and 8-2, respectively.

Fig. 20 compared the exhaust air temperature distribution of Rack B4 in cases 1, 8-1, and 8-2. Compared to Case 1, whether the SAT is set to 23 □ or 23.5 □, the heat accumulation in the lower part of the rack is mitigated to varying degrees. The heat accumulation in the top part of the rack deteriorates slightly in Case 8-1, while it deteriorates moderately in Case 8-2. However, the deterioration of the heat accumulation in both cases 8-1 and 8-2 is acceptable because the upper heat accumulation alleviates the lower heat accumulation. In addition, compared to the heat accumulation in the lower part of Rack B4 in Case 1, the heat accumulation in the upper and lower Rack B4 of cases 8-1 and 8-2 is more moderate.

Thus, both Case 8-1 and Case 8-2 have a better temperature distribution than Case 1. In addition, the heat accumulation phenomenon in Case 1 is also mitigated in cases 8-1 and 8-2. However, the temperature distribution and heat accumulation mitigation effect in Case 8-1 is much better than that in Case 8-2.

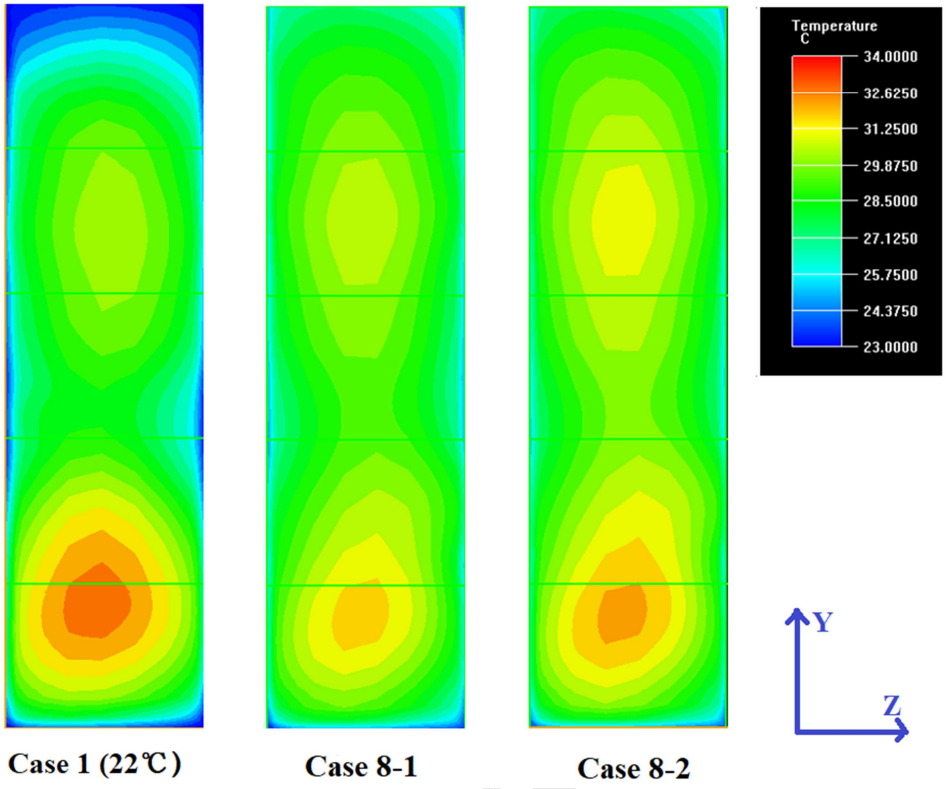

Fig. 20. The temperature distribution of Rack B4 in cases 1, 8-1, and 8-2.

The exhaust air mean temperature and rack hotpot temperature in cases 1, 8-1, and 8-2 are shown in **Fig. 21**. The mean temperature increases with the rise in SAT. A new evaluation index of optimization model performance is proposed, which is defined as the ratio of the rack mean exhaust air temperature difference between the optimization and original model to the SAT difference between them. The new evaluation index is named the MS index, and the equation is shown in **Equation 4**. The MS index is inversely proportional to the SAT difference between the optimization and original model, while it is proportional to the mean exhaust air temperature difference between the optimization and original model. Thus, the bigger the MS index, the higher the thermal distribution and cooling efficiency. In Case 8-1, the SAT rises by 1 □, but the mean temperature rises by only 0.4 □. However, when the SAT rises by 1.5 □, the mean temperature rises from 28.9 □ to 29.8 □ by 0.9 □. The MS index in Case 8-1 is 0.4, and in Case 8-2 it is 0.6. Thus, Case 8-1 has better thermal distribution and cooling efficiency than Case 8-2 in terms of the MS index.

As shown in **Fig. 21**, the temperature of the rack hotspot is lowest in Case 8-1, reducing by 1.2 K compared to that in Case 1. Although the temperature of the rack hotspot in Case 8-2 also falls by 0.6 K, the temperature drop is not as obvious as in Case 8-1. Thus, Case 8-1 performed better than Case 8-2 in terms of thermal distribution, heat accumulation mitigation effect, cooling efficiency, and rack hotspot.

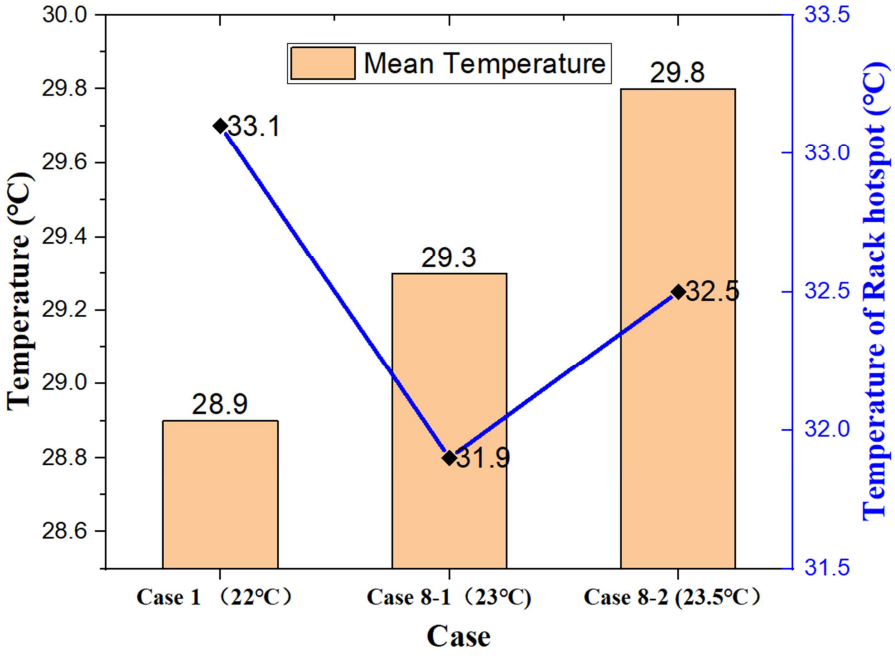

Fig. 21. The mean temperature and temperature of rack hotspot of Rack B4 in cases 1, 8-1, and 8-2.

$$MS = \frac{MT_{om} - MT_o}{SAT_{om} - SAT_o} \quad (4)$$

$$Q = cp \cdot m \cdot \Delta t \quad (5)$$

$$m = \rho \cdot V \quad (6)$$

$$V = v \cdot A \quad (7)$$

$$\Delta t = SAT_{C8-1} - SAT_{C1} \quad (8)$$

$$Q = cp \cdot \rho \cdot v \cdot A \cdot (SAT_{C8-1} - SAT_{C1})$$

$$1\frac{kJ}{kg \cdot K} \cdot 1.293\frac{kg}{m^3} \cdot 5.33\frac{m}{s} \cdot 0.45m^2 \cdot 2 \cdot (23℃ - 22℃) = 6.2\ kWh \quad (9)$$

The electricity use of CRACs should decrease due to the rise of SAT in Case 8-1, thus **Equations 5-8** are used to calculate the electricity saving of Case 8-1 compared to Case 1. **Equation 9** shows the hourly cooling energy saving of 6.2 kWh in Case 8, which means approximate 150 kWh/day cooling energy will be saved in this DC. According to **Table 2**, the COP of each CRAC is around 1.53. Thus, the total electricity saving of CRACs is about 98 kWh/day.

To sum up, Case 8-1 performed the best in terms of thermal distribution, heat accumulation mitigation effect and rack hotspot. In addition, it can also improve the cooling efficiency and save electricity use of 98 kWh/day in this DC.

5. Conclusion

The higher heat load densities of servers increase the risk of electronics overheating and threaten its operation safety. Simultaneously, higher loads increase the energy consumption in data centers. Thus, optimization of airflow management and cooling efficiency improvement in a data center (DC) have gotten more attention. This paper introduced and analyzed a new concept where an under-floor air supply (UFAD) system with cold aisle containment (CAC) is replaced by a new in-rack UFAD system called an in-rack cold aisle (IR-CA). The simulation model was validated by an on-site measurement, while the numerical and experimental results of both temperatures and velocities were in good agreement. The study is divided into eight cases with seven different dimensions for the rack air inlet (2.2 m × 0.6 m, 0.2 m × 0.6 m, 0.3 m × 0.6 m, 0.4 m × 0.6 m, 0.5 m × 0.6 m, 0.6 m × 0.6 m, and 0.7 m × 0.6 m), while an additional partition plane is placed in Case 8 with a 0.6 m × 0.6-m rack air inlet. The thermal distribution is compared and analyzed in the eight cases, while the cooling efficiency and energy saving is compared between the original and optimal cases. The conclusions in this paper are drawn and shown as follows:

(1) The replacement of a UFAD system with CAC by an in-rack UFAD system (IR-CA) can improve the thermal distribution when the width of IR-CA is larger than 0.3 m.

(2) Although the thermal distribution in Case 6 with 0.6 m × 0.6 m IR-CA is much improved compared to cases 1–5 and 7, the optimal thermal distribution is achieved in Case 8 with a 0.6 m × 0.6 m IR-CA and a partition plane. Under the circumstances of Case 8, the maximum temperature drop of a rack hotspot can reach 2.4 K.

(3) When the SAT is set to 23□ and 23.5□ in Case 8-1 and 8-2, respectively, the thermal distribution and rack hotspot are still better than those in Case 1. However, Case 8-1 performed much better than Case 8-2 in terms of thermal distribution and rack hotspot temperature.

(4) The application of a 0.6 m × 0.6 m IR-CA and a partition plane in Case 8 with SAT of 23 □ can achieve about 98 kWh/day electricity saving in this DC.

(5) A new evaluation index named the MS index is proposed and defined as the ratio of the rack mean exhaust air temperature difference between the optimization and original model to the SAT difference between them. The bigger the MS index, the better the temperature distribution and cooling efficiency.

Also, there are some limitations in this paper. The parameters set in the numerical model cannot be completely consistent with the actual situation, contributing to inevitable deviation between the simulation and experimental results. In addition, the results may only be applicable to the rack whose

heat accumulation is in the lower part, while for the racks with heat accumulation in the middle and top part, the optimization effect of the IR-CA should be further studied. Last but not least, the results are applicable for the racks only with 2 U servers. However, the optimization effects for the rack with 1 U, 4 U, 7U and other servers on the airflow and temperature distribution should be further investigated.

Acknowledgement

We acknowledge the help from the Information Center of Nanjing Tech University for providing on-site experimental sites.

References

[1] A. Costa, M.M. Keane, J.I. Torrens, E. Corry, Building operation and energy performance: Monitoring, analysis and optimisation toolkit. Applied Energy 101 (2014) 310–316.

[2] J. Wang, Q. Zhang, Y. Yu, An advanced control of hybrid cooling technology for telecommunication base stations, Energy and Buildings 133 (2016) 172–184.

[3] Data Center Energy Consumption Trends. U.S. Department of Energy. Retrieved 2010-06-10.

[4] J.G. Koomey, Growth in Data Centre Electricity Use 2005 to 2010, Analytics Press, Oakland, CA, 2011.

[5] Z. Chkirbene, A. Gouissem, R. Hadjidi, S. Fougou, R. Hamila, Efficient techniques for energy saving in data center networks Zina, Computer Communications 129 (2018) 111–124.

[6] R. Buyya, A. Beloglazov, J.H. Abawajy, Energy-efficient management of data center resources for cloud computing: a vision, architectural elements, and open challenges, CoRR abs/1006.0308 (2010). http://arxiv.org/abs/1006.0308.

[7] Y. Kwon, A study on the evaluation of ventilation system suitable for outside air cooling applied in large data center for energy conservation, Journal of Mechanical Science and Technology 30 (5) (2016) 2319–2324.

[8] S.A. Nada, A.M.A. Attia, K.E. Elfeky, Experimental study of solving thermal heterogeneity problem of data center servers, Applied Thermal Engineering 109 (2016) 466–474.

[9] S.A. Nada, M.A. Said, Effect of CRAC units layout on thermal management of data center, Applied Thermal Engineering 118 (2017) 339–344.

[10] H. Zhang, S. Shao, H. Xu, H. Zou, C. Tian, Free cooling of data centers: A review. Renewable and Sustainable Energy Reviews 35 (2014) 171–82.

[11] R. Gao, C. Wang, A. Li, S. Yu, B. Deng, A novel targeted personalized ventilation system based on the shooting concept, Building and Environment 135 (2018) 269–279.

[12] R. Gao, K. Liu, A. Li, Z. Fang, B. Cong, Biomimetic duct tee for reducing the local resistance of a ventilation and air-conditioning system, Building and Environment 128 (2018) 130–141.

[13] X. Yuan, X. Tao, J. Liu, Y. Wang, R. Kosonen, X. Xu, Experimental and numerical investigation of an airflow management system in data center with lower-side terminal baffles for servers, Building and Environment 155 (2019) 308–319.

[14] A. Khalaj, S.K. Halgamuge, A review on efficient thermal management of air- and liquid-cooled data centers: from chip to the cooling system, Applied Energy 205 (2017) 1165–1188.

[15] X. Yuan, Y. Wang, J. Liu, X. Xu, X. Yuan, Experimental and numerical study of airflow distribution optimisation in high-density data center with flexible baffles, Building and Environment 140 (2018) 128-39.

[16] S. Zimmermann, I. Meijer, M.K. Tiwari, S. Paredes, B. Michel, D. Poulikakos, Aquasar: A hot water-cooled data center with direct energy reuse, Energy 43(1) (2012) 237–45.

[17] Q. Nie, Y. Joshi, Reduced order modeling and experimental validation of steady turbulent convection in connected domains, International Journal of Heat Mass Transfer 51 (2008) 6063–6076.

[18] S.D. Christy, S. Abimannan, Energy efficient free cooling system for data centers. In: Cloud computing technology and science (CloudCom). 2011 IEEE third international conference on; 2011. p. 646–651.

[19] J. Wang, Q. Zhang, S. Yoon, Y. Yu, Reliability and availability analysis of a hybrid cooling system with waterside economizer in data center, Building and Environment 148 (2019) 405–416.

[20] J. Wang, Q. Zhang, S. Yoon, Y. Yu, Impact of uncertainties on the supervisory control performance of a hybrid cooling system in data center, Building and Environment 148 (2019) 361–371.

[21] S.W. Ham, J.S. Park, J.W. Jeong, Optimum supply air temperature ranges of various air-side economizers in a modular data center, Applied Thermal Engineering 77 (2015) 163–79.

[22] E. Oró, A. Garcia, J. Salom, Experimental and numerical analysis of the air management in a data center in Spain, Energy and Buildings 116 (2016) 553–61.

[23] S.A. Nada, M.A. Said, M.A. Rady, CFD investigations of data centers' thermal performance for different configurations of CRACs units and aisles separation, Alexandria Engineering Journal 55 (2016) 959–971.

[24] R.R. Schmidt, M. Lyengar, Comparison between underfloor supply and overhead supply ventilation designs for data center high-density clusters, ASHRAE Transactions 13 (2007) 115–125.

[25] V. Sorell, S. Escalante, J. Yang, Comparison of overhead and underfloor air delivery systems in a data center environment using CFD modelling, ASHRAE Transactions 111 (2005) 756–64.

[26] J. Cho, T. Lim, K.B. Sean, Measurements and predictions systems in high compute density

(Internet) data centers, Energy and Buildings 41(2009) 1107–15.

[27] S.A. Nada, K.E. Elfeky, Experimental investigations of thermal managements solutions in data centers buildings for different arrangements of cold aisles containments, Journal of Building Engineering 5 (2016) 41–49.

[28] V.K. Arghode, P. Kumar, Y. Joshi, T. Weiss, G. Meyer, Rack level modeling of airflow through perforated tile in a data center, Journal of Electronic Package 135 (3) (2013) 030902.

[29] T. Ding, H. Cao, Z. He, Z. Li, Experiment research on influence factors of the separated heat pipe system, especially the filling ratio and Freon types, Applied Thermal Engineering 118 (2017) 357–64.

[30] Y. Ma, G. Ma, S. Zhang, F. Zhou, Cooling performance of a pump-driven two-phase cooling system for free cooling in data centers. Applied Thermal Engineering 95 (2016) 143–149.

[31] J Siriwardana, S Jayasekara, S.K. Halgamuge, Potential of air-side economizers for data center cooling: a case study for key Australian cities. Applied Energy 2013;104: 207–19.

[32] A. Almoli, A. Thompson, N. Kapur, J. Summers, H. Thompson, G. Hannah, Computational fluid dynamic investigation of liquid rack cooling in data centers, Applied Energy 89 (2012) 150–155.

[33] I.N. Wang, Y. Tsui, C. Wang, Improvement of airflow distribution in a container data center, Energy Procedia 75 (2015) 1819 – 1824.

[34] J. Choi, Y. Kim, A. Sivasubramaniam, J. Srebric, Q. Wang, J. Lee, A CFD-Based Tool for Studying Temperature in Rack-Mounted Servers Computers, IEEE Trans. 57(8) (2008) 1129–1142.

[35] L. Phan, B. Hu, C.X. Lin, An evaluation of turbulence and tile models at server rack level for data centers, Building and Environment 155 (2019) 421–435.

[36] E. Wibron, A.L Ljung, T.S. Lundström, Computational Fluid Dynamics Modelling and Validating Experiments of Airflow in a Data Center, Energies 11 (2018) 644; doi:10.3390/en11030644.

[37] J. Abanto, D. Barrero, M. Reggio, Airflow modelling in a computer room, Building and Environment 39 (2004) 1393-402.

[38] Z. Song, Thermal performance of a contained data center with fan-assisted perforations, Applied Thermal Engineering, 102 (2016) 1175-84.

[39] M. Iyengar, R.R. Schmidt, H. Hamann, J. VanGilder, January). Comparison between numerical and experimental temperature distributions in a small data center test cell, ASME 2007 InterPACK Conference Collocated with the ASME/JSME 2007 Thermal Engineering Heat Transfer Summer Conference, American Society of Mechanical Engineers, 2007, pp. 819–826.

[40] Z. Song, B. Murray, B. Sammakia, A dynamic compact thermal model for data center analysis and control using the zonal method and artificial neural networks, Applied Thermal Engineering 62

(2014) 48-57.

[41] J.W. VanGilder, Z.M. Pardey, P. Bemis, D.W. Plamondon, Compact modeling of data center raised-floor-plenum stanchions: pressure drop through sparse tube bundles, Thermal and Thermomechanical Phenomena in Electronic Systems (ITherm), 2016 15th IEEE Intersociety Conference on, IEEE, 2016, May, pp. 1148–1155..

[42] J.Z. Zhai, K.A. Hermansen, S. Al-Saadi, The development of simplified rack boundary conditions for numerical data center models, ASHRAE Transact. 118 (2) (2012).

[43] L. Phan, C.X. Lin, A multi-zone buildings energy simulation of a data center model with hot and cold aisles, Energy and Buildings. 77 (2014) 264-276.

[44] J. Ni, B. Jin, B. Zhang, X. Wang, Simulation of Thermal Distribution and Airflow for Efficient Energy Consumption in a Small Data Centers, Sustainability 9 (664) (2017) doi:10.3390/su9040664.

[45] L. Phan, C. Lin, Reduced order modeling of a data center model with multi-parameters, Energy and Buildings 136 (2017) 86–99.

[46] S.A. Alkharabsheh, B.G. Sammakia, S. K. Shrivastava, Experimentally Validated Computational Fluid Dynamics Model for a Data Center With Cold Aisle Containment, Journal of Electronic Packaging, 137 (2015) 021010-1.

[47] K. Zhang, X. Zhang, S. Li, G. Wang, Numerical study on the thermal environment of UFAD system with solar chimney for the data centre, Energy Procedia 48 (2014) 1047–1054.

[48] L. Silva-Llanca, A. Ortega, K. Fouladi, M.D. Valle, V. Sundaralingam, Determining wasted energy in the airside of a perimeter-cooled data center via direct computation of the Exergy Destruction, Applied Energy 213 (2018) 235-46.

[49] S. Nada, H. El-Batsh, H. Elattar, N. Ali, CFD investigation of airflow pattern, temperature distribution and thermal comfort of UFAD system for theatre buildings applications, Journal of Building Enineering 6 (2016) 274–300.

[50] J. Siriwardana, S. Halgamuge, T. Scherer, W. Schott, Minimizing the thermal impact of computing equipment upgrades in data centers, Energy and Buildings 50 (2012) 81–92.

[51] X. yuan, X. Xu, Y. Wang, J. Liu, R. Kosonen, H. Cai, Design and validation of an airflow management system in data center with tilted server placement, Applied Thermal Engineering 164 (2020) 114444.

Highlights：

A new concept of in-rack UFAD system and in-rack cold aisle (IR-CA) is proposed

The thermal distribution can be improved when the width of IR-CA is larger than 0.3 m.

The optimal thermal distribution appears in the case of 0.6 m× 0.6 m IR-CA with partition plane.

The optimal model with SAT increased by 1 ℃ can still have better thermal distribution than the original model.

Approximate 98 kWh/day electricity can be saved in the optimal model.

Declarations of interest: none

Jinxiang Liu, Professor
Address: *No. 200, North Zhongshan Road, Gulou district, Nanjing City, Jiangsu Province, P.R. China*
Ph: *+86 188-5177-8187*
E-mail: *jxliu@njut.edu.cn*